Article

High-resolution mapping of substantia nigra in Parkinson's disease using 7 tesla magnetic resonance imaging

Check for updates

Christopher F. Madelung[1,2], Annemette Løkkegaard[2,3], Søren A. Fuglsang[1], Marta M. Marques[1], Vincent O. Boer[1], Kristoffer H. Madsen[1,4], Anne-Mette Hejl[2,3], David Meder[1,5] ✉ & Hartwig R. Siebner[1,2,3,5] ✉

Parkinson's disease causes a progressive loss of dopaminergic neurons and iron accumulation in the substantia nigra pars compacta. Using ultra-high field magnetic resonance imaging (MRI) at 7 tesla in 43 Parkinson's patients and 24 healthy controls, we analyzed the voxel-wise pattern of structural disintegration of dopamine neurons with neuromelanin-sensitive MRI, along with assessing iron accumulation using R2* and quantitative susceptibility mapping (QSM). We also explored correlations between these measures and the severity of residual motor symptoms in the on-medication state and other clinical variables. Differences were most notable in the nigrosomes within the pars compacta, with patients showing reduced neuromelanin signals and increased QSM values. Severity and asymmetry of motor symptoms correlated with higher R2* and QSM values in nigrosome N1. Thus, ultra-high field MRI provides high-resolution maps of various aspects of the underlying neurodegenerative process which reflect individual motor impairment in Parkinson's disease.

In Parkinson's disease (PD), the progressive neurodegeneration of dopaminergic neurons in the pars compacta of the substantia nigra (SNc) leads to the characteristic motor symptoms. Diagnosis primarily relies on clinical criteria, oftentimes aided by nuclear imaging of the dopamine system. While magnetic resonance imaging (MRI) is predominantly used to rule out other potential diagnoses, quantitative MRI techniques have been increasingly used in research to assess nigral pathology in PD. These MRI techniques show strong potential as future biomarkers to aid diagnosis, track disease progression and gain further insight into the relation between individual symptomatology and the spatial pattern of neuropathology[1,2].

Quantitative structural MRI can in patients with PD visualize two key features of the neurodegenerative process in the SNc. The first feature is the structural loss of neuromelanin (NM) containing dopamine neurons which give the region its characteristic macroscopic appearance as the "black body" (i.e., substantia nigra)[3–5]. NM-sensitive MRI techniques thus provide in-vivo markers for the integrity of dopaminergic SNc neurons[6]. The relationship between NM-sensitive MRI and both nigral NM content as well as striatal dopamine innervation has been confirmed in post-mortem and in-vivo studies in healthy individuals, but also PD patients[6–9].

Another structural feature of PD is the excessive regional accumulation of iron in the SNc[10–13]. MRI can detect local iron concentration because iron influences the magnetic susceptibility and relaxation behavior[14–16]. Post-processing of T2*-weighted images to R2*-maps and quantitative susceptibility maps (QSM) allows for quantitative in-vivo assessment of iron tissue concentration in Parkinson's disease[17–21]. Although both, R2* and QSM, are iron-sensitive, they are affected differently by tissue and MRI properties. For instance, R2* also reflects regional myelination and is more sensitive to non-local field disturbances. Thus, their magnitude and distribution are correlated, but not identical[22].

These two features of PD, the decrease in NM and the increase in iron concentration, occur at the same time, but are also interconnected. While being essential for cell function in normal amounts, excessive iron concentrations generate harmful reactive oxygen species. There exists a direct dependency between iron and NM where iron is crucial for NM synthesis and NM chelates iron, acting as the primary iron storage site in the SNc[10–13]. When iron exceeds the chelation capacity of NM, it leads to increased free radical formation, contributing to nigrostriatal neurodegeneration[13,23]. This creates a detrimental cycle in PD, where the loss of NM-containing neurons releases chelated iron, exacerbating its neurotoxic effects. The regional

[1]Danish Research Centre for Magnetic Resonance, Center for Functional and Diagnostic Imaging and Research, Copenhagen University Hospital Amager and Hvidovre, Copenhagen, Denmark. [2]Department of Neurology, Copenhagen University Hospital Bispebjerg and Frederiksberg, Copenhagen, Denmark. [3]Department of Clinical Medicine, University of Copenhagen, Copenhagen, Denmark. [4]Department of Applied Mathematics and Computer Science, Technical University of Denmark, Kgs., Lyngby, Denmark. [5]These authors contributed equally: David Meder, Hartwig R. Siebner. ✉e-mail: davidm@drcmr.dk; h.siebner@drcmr.dk

patterns of iron accumulation and NM loss and their link to clinical symptoms, remain poorly understood[23,24]. One aim of this study was therefore to map the difference and overlap of the spatial pattern of NM- and iron-sensitive MRI in the SNc in PD.

One key structure where these processes co-occur is the nigrosome-1 (N1) sub-region in the SNc which has a high density of dopaminergic neurons and shows prominent cell loss in Parkinson's disease[3,4]. NM-sensitive MRI has previously revealed signal reduction in the postero-lateral SNc, corresponding to N1[20,24–26]. In iron-sensitive MRI, the N1 appears as a hyperintense "swallow tail sign" in healthy individuals because of its relatively low iron content[27]. The "swallow tail sign" disappears in PD, indicating iron accumulation in the dorsolateral SNc[27–30]. The observed correlations between NM- and iron-based MRI signals in N1 and the more ventromedially placed N2 suggest a spatial overlap of NM loss and iron accumulation in Parkinson´s disease in the nigrosomes[20,24,25]. However, in other parts of the SN one might expect differences in the regional expression of NM loss and iron accumulation. For instance, the substantia nigra pars reticulata (SNr) lacks NM-containing dopamine neurons but shows high iron concentrations in Parkinson's disease[31,32].

Structural changes in the SN, as revealed by MRI, are closely linked to the severity of parkinsonism. Numerous studies have shown that the severity of motor symptoms, assessed in the OFF-medication state, correlates with reduced NM signal or increased iron content in the SN[9,17,21,31,33–35]. However, studies on the relationship between motor symptoms in the ON-medication state and nigral NM loss and iron accumulation showed mixed results, with some finding significant correlations[31,34,36–38] and others not[20,39–41]. In this study, we used ultra-high field 7T MRI to compare the spatial patterns of NM loss and iron accumulation in the SNc and explored which of the MRI modalities best reflected the severity and asymmetry of motor impairment in the ON-medication state.

We recruited 49 patients with PD and 27 healthy, age-matched controls and performed NM-sensitive magnetization transfer-weighted (MTw) and iron-sensitive R2* and QSM MR images and computed voxel-wise difference maps between the two groups. We then tested for associations between individual motor symptom severity and MR signal change in the N1 as well as the rest of the SN. Finally, we explored voxel-wise correlations between the three acquired MR-modalities in each group separately.

Results

Clinical and imaging data

Demographical and clinical characteristics of the study population are summarized in Table 1. Of the 49 patients recruited, 3 were excluded due to contraindications to 7T MR-scanning, 1 due to unreported neurological conditions, 1 due to incidental findings on structural MRI and 1 due to generally poor scan quality across all modalities. Two of the 27 healthy controls were excluded due to initially unreported neurological conditions and another healthy control participant dropped out before the MRI scan session. Thus, the resulting study population consisted of 43 patients and 24 healthy controls.

The PD group and the healthy control group did not differ in age (Wilcoxon rank-sum, $Z = 550$, $p = 0.661$) or gender ($\chi^2(1) = 0.37$, $p = 0.543$) (see Table 1 for distribution in sub-samples). The PD group spanned a large range in terms of disease duration and time since symptom onset (0–17 years and 1–18 years respectively) and included patients with mild to moderate disease (Hoehn & Yahr stages 1–3). In the PD group, motor laterality was well balanced with 18 and 25 patients most severely affected in the right and left side respectively. The proportion of scan data available following exclusion of imaging data of poor quality did not differ between groups (NM imaging available in 42 patients and 24 healthy controls ($\chi^2(1) = 2.395$, $p = 1$), R2* imaging available in 32 patients and 21 healthy controls ($\chi^2(1) = 0.901$, $p = 0.342$), QSM imaging available in 36 patients and 23 healthy controls ($\chi^2(1) = 1.152$, $p = 0.283$).

Between-group differences in local neuromelanin and iron content

Voxel-wise analyses of between-group differences of both the NM-maps (MT-weighted neuromelanin contrast-to-noise ratio (MT CNR) maps, Fig. 1a) and the iron-sensitive QSM maps revealed NM loss and iron accumulation centered around the nigrosomes. The QSM maps showed a much broader extent of significant group-differences across the SNc compared to the NM maps. However, there was a clear overlap of NM loss and iron accumulation in a bilateral region corresponding to

Table 1 | Demographics and clinical characteristics

	MT CNR			R2*			QSM		
	PD (N = 42)	HC (N = 24)	p	PD (N = 32)	HC (N = 21)	p	PD (N = 36)	HC (N = 23)	p
Age (years)	67.5 (38, 84)	71.5 (43, 80)	0.557	67 (38.79)	71 (43, 76)	0.623	66.5 (38, 80)	71 (43, 80)	0.33
Sex (male/female)	23/19	16/8	0.49	18/14	15/6	0.41	21/15	16/7	0.55
Time from onset (years)	6.06 (0.980, 18.3)	–	–	5.69 (1.84, 18.3)	–	–	5.69 (1.84, 16.8)	–	–
LED[c] (mg/day)	479 (100, 2140)	–	–	479 (100, 2140)	–	–	460 (100, 2140)	–	–
Most affected side (right/left)	17/25	–	–	12/20	–	–	15/21	–	–
UPDRS-III	23.4 ± 9.27	–	–	24.2 ± 9.20	–	–	24.1 ± 9.34	–	–
NMSS[e]	31.0 (3, 118)	–	–	33.0 (3, 118)	–	–	30.5 (3, 118)	–	–
MoCA[d]	28 (17, 30)	28 (23, 31)	0.37	28 (17, 30)	28 (23, 31)	0.62	28 (17, 30)	28 (25, 31)	0.17
BDI-II[a]	8 (0, 20)	3 (0, 11)	0.001*	9 (0, 20)	3 (0, 11)	0.003*	6.5 (0, 20)	3 (0, 11)	<0.001*
LARS[b]	−22.4 ± 6.09	−25.5 ± 4.93	0.03*	−21.6 ± 5.96	−25.3 ± 4.91	0.02*	−22.4 ± 6.20	−25.5 ± 5.04	0.04*

Between group differences were assessed using Student's *t* test for normally distributed data (data reported as mean ± SD) and Wilcoxon rank-sum test when normal distribution could not be assumed (data reported as median (range)). Between group differences in sex distribution were assessed using Pearson's Chi-squared test with Yates' continuity correction.
*$p < 0.05$.
[a]BDI-II: Beck's Depression Inventory score.
[b]LARS: Lille Apathy Rating Scale score.
[c]LED: Levodopa Equivalent Dose.
[d]MoCA: Montreal Cognitive Assessment score.
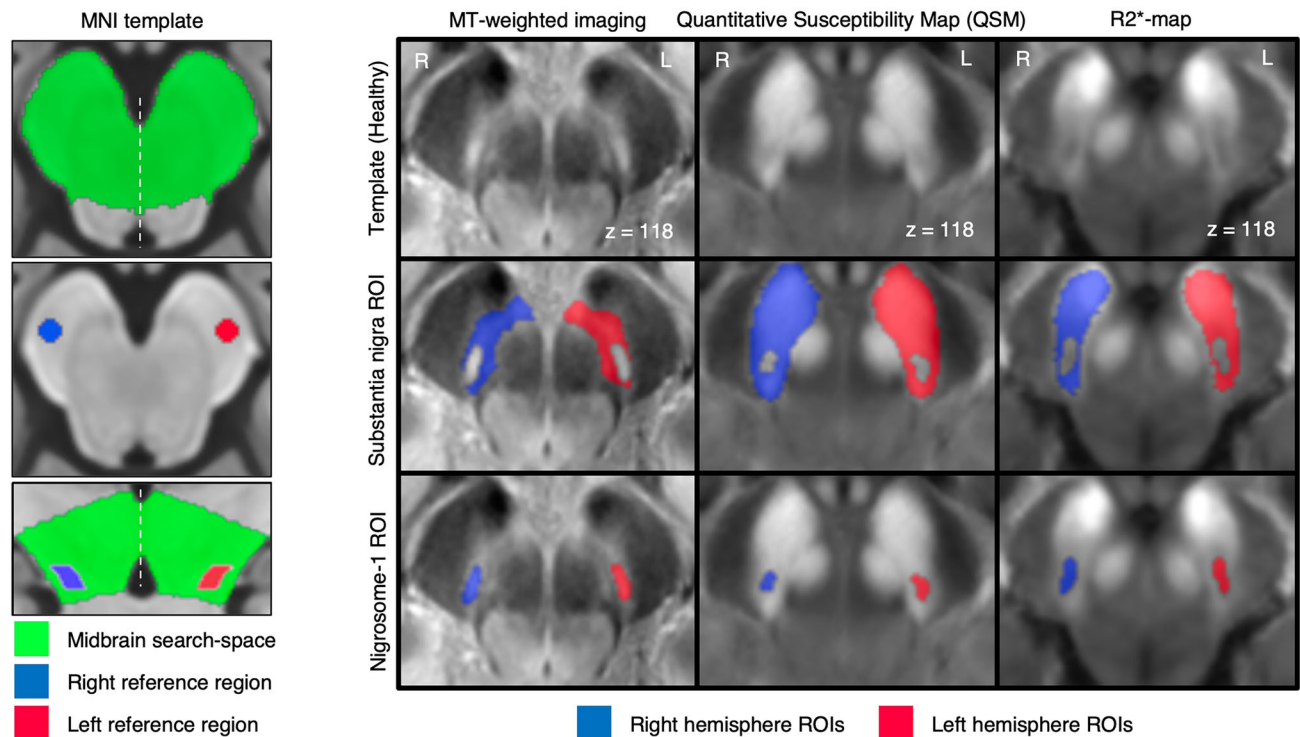[e]NMSS: Non-motor symptom scale score.

a) Search-space and reference regions.   **b) Substantia nigra and nigrosome-1 regions of interest.**

Fig. 1 | Reference regions and regions of interest. a A midbrain search-space (green) and lateralized cylindrical reference regions (blue and red) were manually defined on the MNI-template and used to calculate lateralized MT CNR maps of the midbrain. **b** For the ROI analysis in patients, the ROIs were defined manually on MT-weighted, high-resolution QSM and low-resolution R2* templates constructed by averaging data from all healthy controls. For each modality an ROI was defined for the right (blue) and left (red) SN and N1 (based on dorsal nigral hyperintensity, low quantitative susceptibility and low R2* for the MTw, QSM and R2* modalities respectively). Mean MT CNR, R2* and QSM values were extracted from each lateralized ROI for the assessment of correlations with contralateral motor severity and motor asymmetry.

the location of N1 (Fig. 2b, c, z-coordinates 116-124). The assumption that this region corresponds to the N1 was corroborated by the group template that was constructed from MT-weighted images from healthy controls. This template displayed the well described clustering of NM-containing dopamine neurons into nigrosomes (Fig. 1b). The NM-loss was accordingly located within the hyperintense dorsolateral cluster corresponding to the location of the N1. Furthermore, patients displayed voxels with higher quantitative susceptibility ventromedially in a cluster corresponding to the location of N2 (Fig. 2c, z-coordinates 112-124). The NM contrast was significantly decreased in a similar, albeit smaller area and only in the right SNc (Fig. 2b, z-coordinates 112-116). Additionally, patients had lower NM contrast in a bilateral area just medial to the N1 in the dorsal tier of SNc (Fig. 2b, z-coordinate 116) corresponding to the location of N4. R2* values were also increased in regions corresponding to N1 and N2, but the clusters showing a between-group difference were more confined and differences did not survive correction for multiple comparisons (Fig. 2d).

Associations between the MRI-based read-outs and measures of disease severity

Given the predominant cell loss in N1 in PD and its clear delineability in the templates of all imaging modalities in the healthy control group (Fig. 1), we analyzed associations between disease severity and MRI readouts separately for the N1 and the rest of the substantia nigra (Table 2 and Fig. 3a). We found significant associations between iron-sensitive modalities and residual motor severity where higher contralateral R2* values in the SN and N1 as well as higher QSM values in the N1 were associated with higher motor severity. More specifically, higher UPDRS-III scores were significantly associated with higher contralateral R_2* values in the SN ($t(30.84) = 4.06$,

$adj.p = < 0.001$, 0.51 (±0.12) 1/s increase in R_2* for each one-point increase in UPDRS-III) and N1 ($t(34.49) = 5.14$, $adj.p < 0.001$, 1.02 (±0.20) 1/s increase in R_2* for each one-point increase in UPDRS-III). Similarly, higher UPDRS-III scores were significantly associated with increased contralateral quantitative susceptibility in the N1 ($t(40.66) = 2.85$, $adj.p = 0.024$, 1.22 (±0.43) ppb increase in quantitative susceptibility for each one-point increase in UPDRS-III). No significant associations were found between UPDRS-III scores and NM in the SN ($t(56.38) = -0.89$, $adj.p = 0.506$) or N1 ($t(53.98) = -1.76$ $adj.p = 0.145$).

Evaluating associations between MRI modalities and LED, a trend was observed where lower SN NM contrast was related to higher dopaminergic deficiency, but this did not survive correction for multiple comparisons ($t(36.52) = -2.26$, $p = 0.024$, $adj.p = 0.081$) and no effects on LED dose were found in the remaining models (Fig. 3c).

Since clinical symptoms might be susceptible to the variability in disease duration, we also tested models including disease duration as additional factor. This did not change the reported above (Supplementary Table 2).

UPDRS-III scores and LED were not significantly correlated (Supplementary Fig. 2). Further visualization of the data for each hemisphere is provided as scatterplots in Supplementary Fig. 1a, and the full models are presented in Supplementary Table 1.

In an exploratory analysis, we also tested relationships between the asymmetry of motor symptoms and the asymmetry of MRI measures in the SN and N1 for all three modalities (Fig. 3b). Asymmetry in R2* in the N1 and SN were significantly related to asymmetry in residual motor severity (R2* in N1: $t(27) = -4.41$, $adj.p = 0.002$, effect size = -0.949 (±0.215); R2* values in SN: $t(27) = -4.01$, $adj.p = 0.003$, effect size = -0.434 (±0.108)). After correcting for multiple comparisons, neither asymmetry in the N1 nor in the SN in QSM- or NM-imaging were related to asymmetry in motor
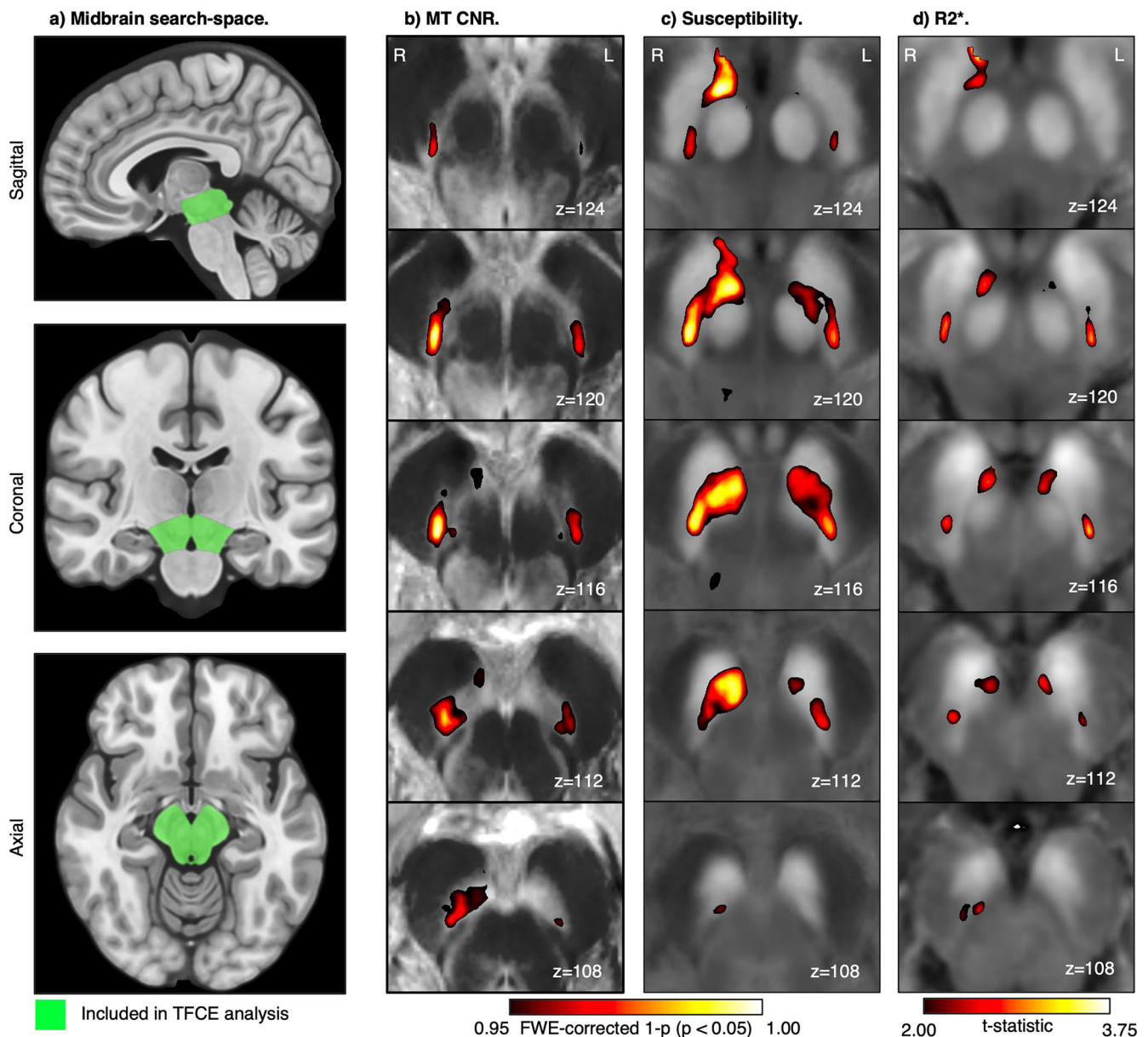
Fig. 2 | Threshold free cluster enhancement (TFCE) of the midbrain. TFCE analyses in a midbrain search-space (ROI) **a** of the between group difference revealed a decrease in MT-weighted contrast to noise ratio (MT CNR) in patients with PD compared to healthy controls in areas corresponding to the bilateral nigrosomes N1 and N4 and right N2, **b** Patients had increased QSM values in areas corresponding to bilateral nigrosomes N1 and N2, **c** No significant voxel-wise difference was found for R2*, **d** Statistical maps in **b** and **c** are thresholded at family-wise error corrected $p < 0.05$. In **d**, the statistical map is thresholded at $t > 2$ for visualization purposes, none of the differences are significant after correction for multiple comparisons.

symptoms. Further information can be found in Supplementary Table 3, a visualization of the data is provided as scatterplots in Supplementary Fig. 1. We again explored whether adding disease duration as a factor changed the results, which again it did not (Supplementary Table 4).

Two-sample t-tests were used to test for differences between patients and healthy participants in midbrain NM (one-tailed testing for lower NM in PD than HC) and iron measures (one-tailed testing for higher susceptibility in PD than HC). The models included mean-centered regressors for age and sex. Significance was established based on a randomization procedure[42] based on voxel-wise threshold-free cluster enhancement (TFCE) statistics[43].

Voxel-wise between modality correlations
Voxel-wise MT CNR was strongly negatively correlated with R2* in antero-medial aspects of the substantia nigra in both patients with PD and healthy controls (Fig. 4A). MT CNR and QSM were also found to correlate negatively in the SN and red nucleus in patients, but voxel-wise correlation was only significant in a few voxels in healthy controls (Fig. 4B). Finally, R2* and QSM correlated positively in the majority of the SN and in the red nucleus (Fig. 4C). However, even though both the spatial distribution and the strength of the correlation patterns appears to be different between PD patients and healthy controls (in healthy controls, correlations between MT CNR and QSM appear stronger and more widely spread, but weaker and more confined for the correlations between the other modality pairs), we found no statistical difference between the correlation values in any of the pairwise correlations (Supplementary Fig. 3).

Discussion
In this study, we leveraged the increased signal-to-noise ratio of ultra-high field MRI to investigate the sensitivity of MTw, QSM and R2* maps to detect

Table 2 | Relationship between imaging measures and clinical variables assessed using linear mixed models

| Predictors | Std.Beta | Substantia nigra | | | Nigrosome-1 | | | |
		Std. CI	*t*-statistic	*p* value	Std.Beta	Std. CI	*t*-statistic	*p* value
Linear mixed model, MT CNR								
UPDRS-III[b]	−0.07	−0.24 to 0.09	−0.89	0.380	−0.14	−0.29 to 0.02	−1.76	0.079
LED[a]	−0.28	−0.52 to −0.04	−2.26	**0.024**	−0.23	−0.47 to 0.02	−1.82	0.069
Linear mixed model, R2*								
UPDRS-III[b]	0.15	0.08 to 0.22	4.06	**<0.001***	0.36	0.23 to 0.50	5.14	**<0.001***
LED[a]	0.00	−0.34 to 0.35	0.03	0.977	−0.01	−0.32 to 0.30	−0.04	0.965
Linear mixed model, QSM								
UPDRS-III[b]	0.10	0.00 to 0.20	2.00	0.046	0.21	0.07 to 0.35	2.85	**0.004***
LED[a]	−0.27	−0.60 to 0.07	−1.57	0.116	0.03	−0.25 to 0.31	0.22	0.823

We constructed linear mixed-effects (LME) models to analyze spatially averaged signal intensities within regions of interest (ROIs). Data from both hemispheres (left and right) were included. Separate models were created for each imaging modality (MT CNR, R2* or QSM) and each anatomical structure (i.e., substantia nigra and nigrosome-1). Fixed effects in the models included hemisphere, age, LED score, sex, and the UPDRS-III score for the contralateral hand. Random intercepts were included for each subject. The models were specified as follows:
ROI_{mean}_hemisphere ~ 1 + UPDRS-III$_{contralateral\ hand}$ + hemisphere + LED + age + sex + (1 | subject)", where ROI_{mean}_hemisphere represents the spatially averaged signal in a given hemisphere for a specific anatomical structure.
Standardized beta-coefficients with 95% confidence intervals are reported for each fixed effect term along with the corresponding *t*-statistics and uncorrected *p* values (uncorrected *p* values < 0.05 in bold).
*False discovery-rate adjusted *p* value < 0.05.
[a]LED: Levodopa equivalent dose.
[b]UPDRS-III: Unified Parkinson's Disease Rating Scale, subscore III of side contralateral to ROI.

dopamine neuron loss and iron accumulation in the SN in PD and their relation to motor disability. Disease-induced structural changes in NM and iron signal overlapped in the N1 and N2. NM signal was also reduced in the N4 region, while QSM showed a larger spatial extent of group differences. While R2* maps did not reveal differences in iron signal between groups, this modality showed the strongest relationship with residual motor symptoms.

Patients displayed a bilateral NM loss and increased iron accumulation in the SN. NM loss was mostly confined to the nigrosomes 1, 2 and 4. R2* maps displayed visually comparable patterns of increased iron signal confined to N1 and N2 regions in PD patients, but these differences did not survive correction for multiple comparisons. The reduced NM and increased quantitative susceptibility in nigrosomal subregions are consistent with the findings of recent studies using voxel-wise analysis of iron sensitive MRI[20,25]. We confirm and extend these studies by showing a reduced NM signal in a region corresponding to N4. The loss of NM contrast in N1 matches histopathological findings described by Damier et al.[3] as well as previous neuroimaging studies that subdivided the SNc into subregions[24,26,37]. Together, our results indicate that N1 but also N2 and N4, with their high density of dopaminergic neurons, are the most sensitive regions for MRI mapping of structural changes[44]. Although significant changes in nigrosomes beyond N1, such as N2 and N4, can be detected at field strengths below 7 tesla[25], the majority of significant findings regarding these regions come from ultra-high field MRI studies[20,24,45]. These reports, together with our findings, underscore the potential of ultra-high field MRI systems with their increased signal-to-noise ratio to detect structural disintegration in nigrosomes other than N1.

The spatial overlap of NM reduction and iron accumulation in the N1 and N2 regions supports a link between regional neuronal loss and iron accumulation in PD. Iron is essential for dopamine synthesis, and NM is an end product of the dopamine-iron complex chain involving the oxidization of dopamine by iron[23]. Since NM stores iron, the death of dopaminergic neurons releases iron, leading to a co-localization of NM loss and iron accumulation in PD[23]. This notion is supported by recent post-mortem studies that showed a concomitant loss of dopaminergic neurons in N1 and an increase in both cellular iron and extracellular iron, as well as NM-bound iron[46]. Some in vivo studies also reported this regional co-occurrence of NM loss and iron accumulation[20,24,25,47]. Of note, one study found no correlation[9], but methodological differences make comparisons among studies challenging.

We computed voxel-wise correlations to explore spatial co-expression of NM and the two MR-derived iron signals in patients and healthy controls. Both patients and healthy controls showed high correlations between the NM signal and R2* values in the SNc, suggesting that the two modalities probe similar tissue properties in the healthy and degenerated SN. However, the NM contrast correlated more strongly with regional quantitative susceptibility in patients than in healthy controls, indicating that QSM may better reflect disease-related iron accumulation than R2*. However, none of the differences in correlations between groups were statistically significant (Supplementary Fig. 3), so these interpretations remain speculative and require further investigation with larger datasets.

Beyond the overlap in the N1 and N2 regions, there were some notable differences in the spatial expression of disease-related changes in NM and iron-sensitive MRI measures. Regional quantitative susceptibility increases were more widespread than NM losses, suggesting iron accumulation may precede dopamine neuron loss in the SNc[24]. The different spatial patterns could be due to varying MR sensitivity to NM loss versus iron accumulation. However, our finding of significant NM decrease without iron accumulation in the N4 region argues against lower NM-sequence sensitivity as the sole factor.

While NM-sensitive MTw and QSM maps showed significant group differences, voxel-wise R2* values did not differ between patients and healthy controls. In agreement with previous studies[20,31,38], R2* values in N1 and N2 increased in patients with PD, but these changes were not statistically significant. In our study, R2* maps appeared to be noisier and more prone to artifacts compared to QSM maps. Despite including only R2* maps of acceptable quality, noise in the fitted R2* values likely contributed to the lack of significant differences. Accordingly, previous studies comparing R2* to QSM suggest that QSM might be more sensitive for detecting alterations in nigral iron content[31,40].

While R2* values had low sensitivity for detection of between-group differences, regional R2* maps were more consistently related to residual motor symptoms in the ON-medication state. Both contralateral motor symptoms and motor symptom asymmetry were significantly associated with R2* values in the SN and the N1 region. We therefore infer that R2* maps may be more suited to explore inter-patient differences and their relation to motor dysfunction rather than detecting a deviation in nigral iron content at the group level relative to healthy controls. The finding that nigral iron accumulation is associated with motor symptom severity aligns with some previous studies, both OFF[31,34] and ON medication[38,48], though others

Fig. 3 | Associations between MRI measures and motor severity. Plots show standardized beta-coefficients and confidence intervals for each ROI/ modality combination for each mixed linear model. **a** Associations between MRI-measures in the SN and N1 and motor severity (contralateral UPDRS-III in the ON-medication state), **b** Associations between the asymmetry of MRI-measures and the asymmetry of motor severity. **c** Associations between MRI-measures in the substantia nigra and N1 and LED. * Denotes significant association.

a) Relationship between imaging measures and UPDRS-III.
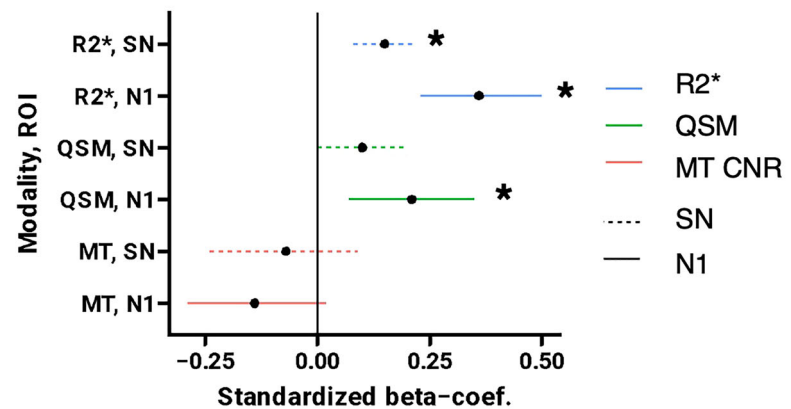
b) Relationship between signal asymmetry and motor asymmetry.
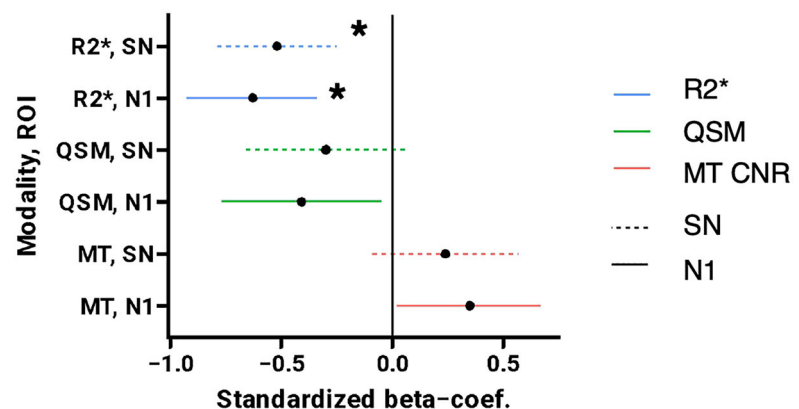
c) Relationship between imaging measures and LED.
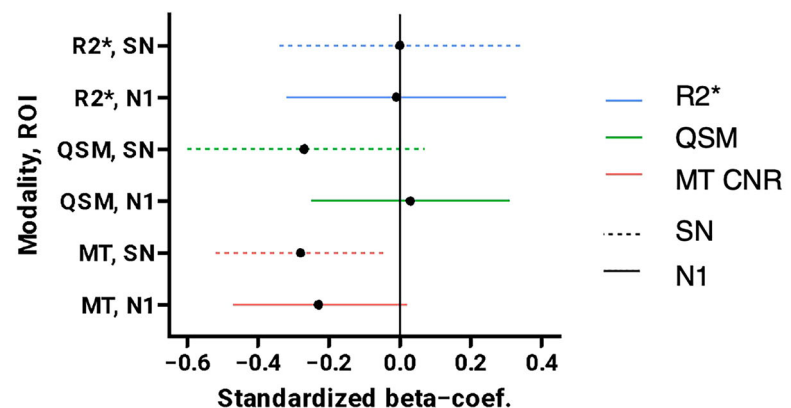
found no association[20,35,39,41]. While R2* and QSM maps are both sensitive to iron, outside N1 only R2* was significantly associated with residual motor severity. When interpreting this finding, it is worth to point out that R2* is also sensitive to other tissue properties, such as myelination and non-local field disturbances[22]. This results in smaller signal differences between patients and healthy controls and reduces the sensitivity for between-group differences. The observed structure-dysfunction relationship might thus reflect a combined effect of PD on iron concentration and other tissue properties in the SN that may render the nigral R2* signal sensitive to variations in residual motor symptoms in the ON-medication state. This hypothesis aligns with the idea that residual motor symptoms ON medication relate to structural changes beyond dopaminergic cell death, but
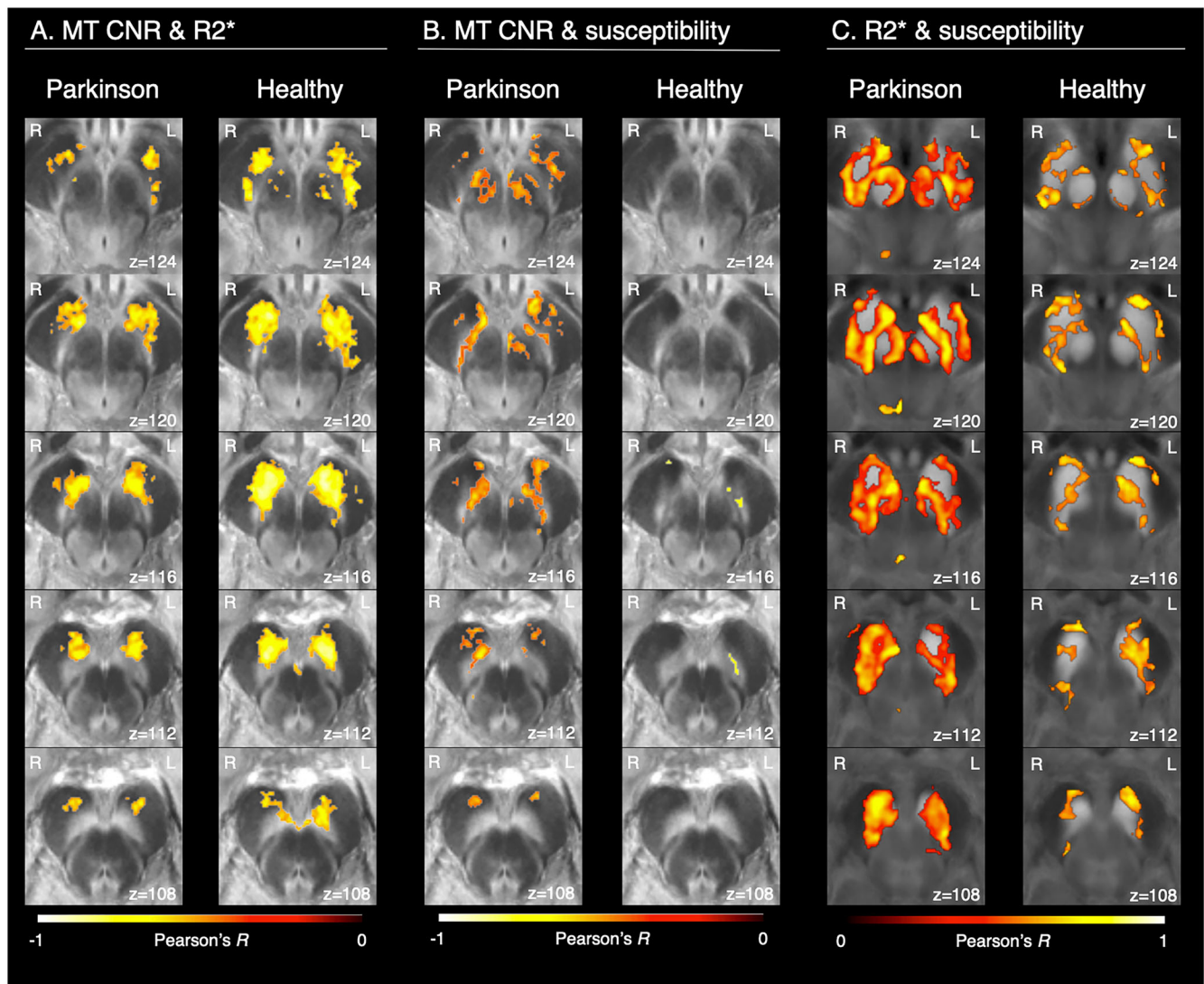
Fig. 4 | Voxel-wise between modality correlations. Voxel-wise correlations between MT CNR, R2* and QSM in patients and healthy controls. Significance was accepted at a threshold of family-wise error rate adjusted $p < 0.05$. Thresholded maps of voxel-wise Pearson's correlation coefficients are presented for **A** MT CNR & R2*, **B** MT CNR & QSM, and **C** R2* & QSM for patients and healthy controls respectively. Maps are overlaid on study specific templates for spatial reference.

more studies are needed to investigate how disease symptoms map onto these different imaging modalities.

While MRI measures of regional iron accumulation were significantly correlated with greater residual motor impairment in the ON-medication state, no significant association was found between decreased NM signal and residual motor impairment in the ON-medication state. It is possible that UPDRS-III scores would have shown a negative correlation with the nigral NM signal if motor impairment had been measured in the OFF-medication state[49]. Previous studies on motor severity and the nigral NM signal yielded conflicting results, with some finding associations OFF[9] and ON medication[36,37] and others finding no associations OFF[33,50] or ON medication[48]. In our data, the NM signal showed a trending association with LED, an indirect measure of dopaminergic degeneration, suggesting that iron accumulation and dopamine cell loss might reflect different aspects of dopaminergic degeneration. However, this association did not survive correction for multiple comparisons, so this interpretation remains speculative.

We used high-resolution 7T MRI to map NM loss and iron accumulation in PD. Imaging of the SN was performed at an unmatched spatial resolution, with MT-weighted images acquired at 0.4 mm in-plane resolution and 1 mm slice thickness. This higher resolution allowed us to create a detailed template demonstrating the anatomical details of the SNc,

surpassing previous studies using 2–3 mm slice thickness[7,26,33,37,50–55]. However, the study still has a number of limitations:

First, while right-left field inhomogeneity has been previously reported for Philips MRI scanners[56,57], we did not observe any right-left difference in image quality. The apparent between-group differences in the three MRI modalities with seemingly more pronounced differences in the right hemisphere are not reflecting significant site-specific differences between groups.

Second, our multimodal mapping approach did not include a diffusion weighted sequence. Especially diffusion measures of unrestricted diffusion, reflecting extracellular space, have been shown to be increased in the SN in PD[2,58,59]. This increase in free water has been attributed to several neuro-biological causes[60] such as cell loss[61,62] or neuroinflammation[63]. The implementation of diffusion-weighted imaging with diffusion measures such as mean diffusivity or apparent diffusion coefficient as well as free water modeling might have provided valuable information about micro- and macrostructural features to gain further insights into the neurobiological causes underlying the differences in spatial distribution and sensitivity to clinical s of our MRI measures.

Third, lacking post-mortem data, we cannot claim with certainty that the hyper- (MTw images)/hypointense (R2* and QSM) region in the

posterolateral SNc that we used for delineating the N1 in healthy controls exclusively reflects the N1. This approach assumes that N1 is a region containing a high density of pigmented neurons and low tissue iron concentration. Healthy controls show a dorsal hyperintense area in the SN on T2*-weighted or QSM scans, creating the characteristic swallow-tail sign, representing a subregion with low iron concentration[27,29,64,65]. It is a matter of ongoing debate, whether this region represents the cluster of dopaminergic neurons termed nigrosome-1[44]. A recent post-mortem study defined the N1 region on histological sections and then applied biophysical modeling to R2* and QSM maps of the SN[66]. The main contributor to R2* relaxation in the N1 was the NM-bound iron, suggesting that a main source of the swallow-tail sign is related to the high concentration of NM containing neurons in the N1. It was argued that the reduced iron signal in N1 might be driven by several counteracting mechanisms with different contributions over the course of PD. Potential mechanisms include an increase in NM-bound iron in surviving dopamine neurons, a reduction in the number of NM positive neurons as well as an increase in ferritin-bound iron outside dopaminergic neurons[66]. Regardless of the terminology applied, the posterior lateral aspect of the SN is an important subregion to study in PD, because histopathological and imaging studies have independently shown that changes in this region scale with clinical severity and distinguish patients with Parkinson's disease from healthy persons[9,17,18,25,28–30,37,45,46,67–74].

Fourth, analyses of associations between clinical scores and MRI measures were conducted in ROIs delineated using healthy control group templates for each modality. Accordingly, we focused on left and right N1 ROIs, as these were clearly delineated on all modalities prior to performing any group-level analyses. Interestingly, cluster-level inferences revealed group differences not only in N1 but also in N2 and N4. Future studies should investigate the relationship between symptom severity and structural changes in N2 and N4. Furthermore, while the N1 regions were similarly located and sized in all three modalities, the spatial extent of the SN differed between modalities. While it would have been possible to define the ROIs using a single modality (e.g., based on the MT-weighted template) and then derive average signal intensities across all three modalities, we chose to test the regions as defined by the acquired images. This approach directly addresses the more clinically relevant question of whether each acquired image modality is sensitive to PD symptoms. Importantly, ROIs were delineated on group templates from healthy controls before conducting the analyses, thus avoiding potential circularity issues.

Fifth, the ROIs on MT-weighted, R2*, and QSM templates likely include different SN subregions. Since the SNr has high iron concentrations, regions defined on R2* and QSM templates likely include SNr voxels. To account for this, we repeated correlation analyses using regions of interest defined on the MT-weighted template. Results were consistent with the main analysis, confirming our conclusions.

Structural 7T MRI of the SN is a valuable tool for high-resolution mapping of NM loss and iron accumulation in Parkinson's disease. Disease-related microstructural changes occur in clusters, with the most prominent changes localized in the nigrosomes. Although dopamine neuron disintegration and iron accumulation are closely related in PD, MR-based mapping of NM loss and iron content provides complementary insights into SN damage. Our cross-sectional results highlight the potential of multi-modal 7T MRI for tracing nigral involvement and delineating structure-dysfunction relationships in PD.

Methods
We recruited 49 patients with PD and 27 healthy, age-matched controls as part of a larger study investigating brainstem changes in Parkinson's disease. Patients were recruited from the Movement Disorders outpatient clinic at the Department of Neurology, Bispebjerg Hospital (Copenhagen, Denmark) and private practice neurology clinics based in the Copenhagen Region. All participants in the Parkinson's disease group were required to have a clinical diagnosis of Parkinson's disease and were additionally required to meet the Movement Disorders Society Clinical Diagnostic Criteria for "Clinically Established Parkinson's disease" or "Clinically

Probable Parkinson's disease"[75]. Exclusion criteria were pregnancy or breastfeeding, history of other neurologic or psychiatric disease, pacemaker or other implanted electronic devices and claustrophobia. Healthy control participants were recruited by online advertisements on www.forsoegsperson.dk and were required to be 18 years or older with no history of neurologic or psychiatric disease and fulfill none of the exclusion criteria mentioned above. The study was approved by the Regional Committee on Health Research Ethics of the Capital Region of Denmark (Record-id: H-18021857). All participants gave their written informed consent to participate in the study which was registered on Clinical-Trials.gov (Identifier: NCT03866044).

Study procedures
Participants underwent a full neurological examination to exclude participants that exhibited symptoms of any neurological condition other than Parkinson's disease. On the day of clinical examination, patients had taken their usual dopaminergic treatment and motor severity was assessed around 10–11 AM in the ON-medication state using the Unified Parkinson's Disease Rating Scale (UPDRS)[76]. UPDRS-III items representing lateralized symptom severity were summed for the right and left extremities respectively. Additionally, we registered age and sex, as well as patients' disease duration, time since onset of motor symptoms and medication status and calculated patients' levodopa equivalent daily dose[77].

Magnetic resonance imaging
Structural MRI data were collected with a Philips Achieva 7T scanner (Philips, Best, The Netherlands) equipped with a 32-channel Nova head coil (Nova Medical, Inc., MA, USA). To assess the integrity of pigmented (neuromelanin containing) SNc neurons, we acquired MT-weighted images using a 3D high-resolution (voxel size = 0.4 × 0.4 × 1.0 mm) ultra-fast gradient echo sequence aligned to the AC-PC line with a field-of-view covering the midbrain and rostral pons (640 × 640 × 34 voxels), echo time/repetition time = 4.1/8.1 ms, flip angle = 7 degrees, 2 averages. MT-saturation was achieved by applying 16 block-shaped pre-pulses at a frequency offset of 2 kHz (flip angle = 278 degrees, duration = 10 ms), acquisition time = 8 min. In MTw imaging, radiofrequency pulses saturate spins of protons in the "macromolecule-bound" pool, thereby enhancing contrast[78,79]. MTw GRE sequences avoid the long scan durations and high specific absorption rates associated with turbo spin echo based NM sensitive imaging at ultra-high field MRI[78]. For coregistration purposes, we also acquired T1-weighted images with identical acquisition parameters to the MT-weighted sequence, but with a 0 degree flip angle for the off-resonance pre-pulses. For the calculation of QSM maps, a high-resolution (voxel size = 0.4 mm isotropic), single-echo, T2*-weighted 3D fast field echo (FFE) sequence was acquired aligned to the AC-PC line with a field of view covering the midbrain and basal ganglia (640 × 640 × 125 voxels), EPI factor 5, 125 axial slices, echo time/repetition time = 15/31 ms, flip angle = 15 degrees, acquisition time = 7 min. A multi-echo, 3D FFE sequence with a lower resolution (voxel size = 1 mm isotropic) was acquired for the calculation of R2*-maps with a field-of-view covering the entire head (164 × 224 × 224 voxels), 164 sagittal slices, 1 signal average, echo time/repetition time = 3.2, 6.6, 10, 13.4, 16.8 & 20.2 ms/23 ms, flip angle = 15 degrees, acquisition time = 14 min. In addition, we acquired T1-weighted, high-resolution (voxel size = 1 mm isotropic) Magnetization Prepared RApid Gradient Echo (MPRAGE) images with a field-of-view covering the entire head (200 × 288 × 288 voxels) realized from a 3D-T1 TFE sequence with a non-selective inversion pulse, echo time/repetition time/inversion time = 2.2/4.9/1300 ms, acquisition time = 3:30 min. Patients were scanned in the ON-medication state to limit tremor-related movement while inside the scanner.

All images and derived quantitative maps were visually inspected and images of low quality due to subject related (e.g., head movements) or technical artefacts (e.g., susceptibility artefacts involving the brainstem and adjacent brain regions) were excluded from further analysis.

Image processing

Quantitative susceptibility maps were calculated from the magnitude and phase images of the single-echo T2*-weighted acquisition using the Multi-Scale Dipole Inversion method implemented in the QSMbox toolbox in Matlab (https://gitlab.com/acostaj/QSMbox), which was extended to also do a dipole inversion on angulated scans[80]. The post-processing consisted of brain masking (BET2) using the magnitude image, phase unwrapping, Laplacian Boundary Value filter (LVB), followed by a variable spherical mean value filter (vSHARP), and finally a multi-scale dipole inversion using default settings apart from the regularization term, which was set to $\gamma = 10^{2.7}$[80–83]. Voxel-wise quantitative R2* maps were calculated from the multi-echo T2*-weighted magnitude images using the Auto-Regression on Linear Operations (ARLO) algorithm for fast mono-exponential fitting[84].

Imaging data were co-registered and normalized to template space using the ANTs software (v. 2.2.0)[85] following a procedure similar to the pipeline used in our previous study[86]: T1-weighted MPRAGE images were up-sampled to a resolution of 0.5 mm isotropic and served as anatomical reference images. These images, as well as high resolution MT-weighted and T1-weighted images were corrected for bias using the ANTs software (N4 bias field correction, 5 resolution levels, number of iterations per level: $50 \times 50 \times 30 \times 20$, convergence threshold: 1×10^{-6}, isotropic sizing for b-spline fitting: 200)[87]. Within-subject co-registration was achieved by rigid-body registration of the high resolution T1-weighted images to the T1-weighted reference scan and by rigid-body registration of the high resolution MT-weighted images to high resolution T1-weighted images and subsequently to the reference images. Within subject co-registration of susceptibility and R2* maps was achieved through rigid-body registration of the first echo from the multi-echo T2*-weighted acquisition to the reference images and the single echo T2*-weighted magnitude image to a combined magnitude image from the multi-echo T2*-weighted acquisition (root sum of squares image created in QSMbox).

A study specific T1-weighted template was created from individual MPRAGE images from 31 patients and 22 healthy control participants using rigid, affine, and nonlinear diffeomorphic registration (greedy symmetric normalization, SyN) with five resolution levels. All participants MPRAGE reference images were normalized to this study specific template using an identical approach as the one used for creating the template. The study specific T1-weighted template was registered to the MNI 0.5 mm ICBM152 (International Consortium for Brain Mapping) T1-weighted, non-linear, asymmetric template again using rigid, affine and non-linear registration to bridge the normalization of individual T1-weighted images[88]. Finally, we concatenated transformations from within-subject registration and to-template normalization to normalize all images to MNI template space for analysis, and created MT-weighted, R2* map and quantitative susceptibility map templates by averaging normalized images from all healthy participants (Fig. 1b, top row).

Calculation of MT-weighted neuromelanin contrast-to-noise ratio (MT CNR) maps was performed in template space in FSL (v. 6.0.4) using the following procedure. A midbrain search-space was manually segmented on the T1-weighted MNI template following the description provided by Iglesias et al.[89] and divided into right and left midbrain search-spaces and two 3.5×4 mm cylindrical reference regions were placed in the right and left crus cerebri using the ITK-SNAP software (v. 3.8.0) (Fig. 1a) similar to the procedure described by Rua et al.[90].

Neuromelanin maps were calculated as contrast to noise ratio (CNR) from normalized MT-weighted images by subtracting the mean signal intensity of the lateralized reference regions ($\text{mean}_{\text{reference}}$) from the voxel signal intensity (Signal Intensity$_{\text{voxel}}$) and dividing by the standard deviation of these reference regions ($\text{SD}_{\text{reference}}$):

$$\text{CNR}_{\text{voxel}} = \frac{\text{Signal Intensity}_{\text{voxel}} - \text{mean}_{\text{reference}}}{\text{SD}_{\text{reference}}}$$

The right and left normalized neuromelanin maps were then masked by the right and left midbrain search-spaces and combined into one volume with neuromelanin values relative to their respective lateralized reference regions.

To test our hypotheses that loss of NM signal and increase in R2* and QSM values should indicate higher disease severity, we assessed the relationships between our two measures of disease severity (levodopa equivalent daily dose (LED) and residual motor severity (UPDRS-III scores in the ON-medication state) and signal intensity across modalities in manually defined regions of interest (ROIs). Regions of interest were manually defined on the three templates (MT-weighted, R2* and QSM) constructed from healthy participants' imaging data. On the MT-weighted template, the SN was segmented based on the visual boundary between the neuromelanin rich hyperintense voxels of the SNc and the surrounding midbrain (25 slices in z-direction), and a bilaterally symmetric area located in the lateral tier of the SNc was defined as a putative nigrosome-1 region-of-interest (12 slices). Similarly, on the R2* and QSM templates, the hyperintense substantia nigra was segmented manually (25/26 slices, respectively), and the bilateral dorsolateral hypointensity, corresponding to the dorsolateral nigral hyperintensity (i.e., the swallow tail sign) on conventional T2*- and susceptibility weighted images, was defined as putative nigrosome-1 regions of interest (18/8 slices respectively). This resulted in a set of SN and nigrosome-1 ROIs specific to each modality defined on an independent set of healthy control data to avoid circularity. Because the ROIs were defined based on high/low intensities in the HC group template, we did not use them for between-group comparisons to avoid bias toward detecting differences. Using HC-derived boundaries to compare voxel intensities between the PD and HC groups would have inherently skewed the analysis toward larger differences.

Statistical analysis

Two-sample t-tests were used to test for differences between patients and healthy participants in midbrain NM (one-tailed testing for lower NM in PD than HC) and iron measures (one-tailed testing for higher susceptibility in PD than HC). The models included mean-centered regressors for age and sex. Significance was established based on a randomization procedure[42] based on voxel-wise threshold-free cluster enhancement (TFCE) statistics[43]. Data were spatially smoothed by convolution with a 1 mm full width at half maximum isotropic Gaussian kernel. Permutation testing was used to control for multiple comparisons over space using TFCE and maximum permutation statistics with 10,000 permutations randomly shuffling group labels. Significance was accepted at a threshold of familywise error-rate adjusted $p < 0.05$. We also explored to what degree the MRI measures were correlated with one another. To this end, we computed Pearson's correlation coefficient across MRI measures across subjects for each voxel. This was done separately for patients and healthy controls. The correlation coefficients were subsequently transformed using Fisher's Z-transform followed by TFCE. A non-parametric null distribution was formed using 10,000 random permutations by randomly shuffling participant labels for one modality. Again, multiple comparisons adjustment was achieved by maximum permutation statistics and significance was accepted at a threshold of familywise error-rate adjusted $p < 0.05$. The analyses were implemented in Python (Python Software Foundation, v. 3.8.3).

We used separate linear mixed-effects models for each MRI modality (Fig. 1b and Supplementary Table 3). The models were fit using the R (R Core Team 2019, v4.0.4) package lme4. We used the mean MRI signal from each ROI from each hemisphere separately as dependent variable. Explanatory variables included fixed effects of interest (UPDRS-III scores contralateral to the ROI and LED), fixed effects of no interest (age, sex and hemisphere) as well as random intercepts for subjects. Patients' age and sex were included since the Parkinson's disease phenotype is linked to both age and sex[91–93]. p values were obtained using the lmerTest package[94]. We also tested whether adding disease duration as fixed effect would affect the results (Supplementary Table 4). Visual inspection of residual plots did not reveal any obvious deviations from homoscedasticity or normality. Statistical tests were two-tailed, and t-statistics and p values for model coefficients were

calculated using Satterthwaite's method. Significance was accepted at false discovery-rate adjusted $p < 0.05$.

Additionally, we explored whether the degree of asymmetry in our imaging measures (asymmetry of signal changes in the SN and nigrosome-1 in neuromelanin, R2* and QSM MR-images) was related to the asymmetry of motor symptoms. Asymmetry of motor severity was calculated by subtracting the sum of UPDRS-III items from the left side of the body (left upper and lower extremity scores) from the sum of UPDRS-III items from the right side of the body (right upper and lower extremity scores). These models included the same regressors as above, but with Δ mean ROI signal (mean signal in right ROI minus mean signal in left ROI) instead of mean ROI signal as dependent variable and excluding the factor 'hemisphere' (Supplementary Table 1). We also tested whether adding disease duration as fixed effect would affect the results (Supplementary Table 2). For all statistical tests, significance was accepted at a threshold of family-wise error rate adjusted $p < 0.05$.

Data availability
The pseudonymized data can only be shared with a formal Data Processing Agreement and a formal approval by the Danish Data Protection agency in line with the requirements of the General Data Protection Regulation.

Abbreviations

ARLO	Auto-Regression on Linear Operations
CNR	contrast to noise ratio
LBV	Laplacian Boundary Value filter
LC	locus coeruleus
MR	magnetic resonance
MRI	magnetic resonance imaging
MT	magnetization transfer
N1/N2/N4	nigrosome 1/2/4
QSM	quantitative susceptibility mapping
R2*	effective transverse relaxation rate
ROI	region of interest
SNc	substantia nigra pars compacta
SNr	substantia nigra pars reticulata
T1	longitudinal relaxation time
T2*	effective transverse relaxation time
TFCE	threshold-free cluster enhancement
UPDRS	Unified Parkinson's disease Rating Scale
vSHARP	variable spherical mean value filter.

References

1. Tolosa, E., Garrido, A., Scholz, S. W. & Poewe, W. Challenges in the diagnosis of Parkinson's disease. *Lancet Neurol.* **20**, 385–397 (2021).
2. Lehericy, S. et al. The role of high-field magnetic resonance imaging in parkinsonian disorders: pushing the boundaries forward. *Mov. Disord.* **32**, 510–525 (2017).
3. Damier, P., Hirsch, E. C., Agid, Y. & Graybiel, A. M. The substantia nigra of the human brain. II. Patterns of loss of dopamine-containing neurons in Parkinson's disease. *Brain* **122**, 1437–1448 (1999).
4. Poewe, W. et al. Parkinson disease. *Nat. Rev. Dis. Prim.* **3**, 17013 (2017).
5. Zecca, L. et al. Substantia nigra neuromelanin: structure, synthesis, and molecular behaviour. *Mol. Pathol.* **54**, 414–418 (2001).
6. Kitao, S. et al. Correlation between pathology and neuromelanin MR imaging in Parkinson's disease and dementia with Lewy bodies. *Neuroradiology* **55**, 947–953 (2013).
7. Cassidy, C. M. et al. Neuromelanin-sensitive MRI as a noninvasive proxy measure of dopamine function in the human brain. *PNAS* **116**, 5108–5117 (2019).
8. Kuya, K. et al. Correlation between neuromelanin-sensitive MR imaging and (123)I-FP-CIT SPECT in patients with parkinsonism. *Neuroradiology* **58**, 351–356 (2016).
9. Isaias, I. U. et al. Neuromelanin imaging and dopaminergic loss in Parkinsonas disease. *Front. Aging Neurosci* **8**, 196 (2016).
10. Dexter, D. T. et al. Increased nigral iron content and alterations in other metal ions occurring in brain in Parkinson's disease. *J. Neurochem.* **52**, 1830–1836 (1989).
11. Riederer, P. et al. Transition metals, ferritin, glutathione, and ascorbic acid in parkinsonian brains. *J. Neurochem.* **52**, 515–520 (1989).
12. Sofic, E., Paulus, W., Jellinger, K., Riederer, P. & Youdim, M. B. H. Selective increase of iron in substantia nigra zona compacta of Parkinsonian brains. *J. Neurochem.* **56**, 978–982 (1991).
13. Griffiths, P. D., Dobson, B. R., Jones, G. R. & Clarke, D. T. Iron in the basal ganglia in Parkinson's disease. An in vitro study using extended X-ray absorption fine structure and cryo-electron microscopy. *Brain* **122**, 667–673 (1999).
14. Mitsumori, F., Watanabe, H., Takaya, N. & Garwood, M. Apparent transverse relaxation rate in human brain varies linearly with tissue iron concentration at 4.7 T. *Magn. Reson. Med.* **58**, 1054–1060 (2007).
15. Duyn, J. H. Studying brain microstructure with magnetic susceptibility contrast at high-field. *NeuroImage* **168**, 152–161 (2018).
16. Lee, H., Baek, S. Y., Chun, S. Y., Lee, J. H. & Cho, H. Specific visualization of neuromelanin-iron complex and ferric iron in the human post-mortem substantia nigra using MR relaxometry at 7 T. *NeuroImage* **172**, 874–885 (2018).
17. Kim, E. Y. et al. Diagnosis of early-stage idiopathic Parkinson's disease using high-resolution quantitative susceptibility mapping combined with histogram analysis in the substantia nigra at 3 T. *J. Clin. Neurol.* **14**, 90–97 (2018).
18. Cheng, Z. et al. Imaging the Nigrosome 1 in the substantia nigra using susceptibility weighted imaging and quantitative susceptibility mapping: an application to Parkinsonas disease. *Neuroimage Clin* **25**, 102103 (2019).
19. Xiao, B. et al. Quantitative susceptibility mapping based hybrid feature extraction for diagnosis of Parkinsonas disease. *Neuroimage Clin* **24**, 102070 (2019).
20. Langley, J. et al. Multimodal assessment of nigrosomal degeneration in Parkinson's disease. *Parkinsonism Relat. Disord.* **80**, 102–107 (2020).
21. Sun, J. et al. Quantitative evaluation of iron content in idiopathic rapid eye movement sleep behavior disorder. *Mov. Disord.* **35**, 478–485 (2020).
22. Betts, M. J., Acosta-Cabronero, J., Cardenas-Blanco, A., Nestor, P. J. & Düzel, E. High-resolution characterisation of the aging brain using simultaneous quantitative susceptibility mapping (QSM) and R2* measurements at 7 T. *NeuroImage* **138**, 43–63 (2016).
23. Zucca, F. A. et al. Interactions of iron, dopamine and neuromelanin pathways in brain aging and Parkinson's disease. *Prog. Neurobiol.* **155**, 96–119 (2017).
24. Biondetti, E. et al. The spatiotemporal changes in dopamine, neuromelanin and iron characterizing Parkinson's disease. *Brain* **12**, awab191 (2021).
25. Sung, Y. H., Noh, Y. & Kim, E. Y. Early-stage Parkinson's disease: abnormal nigrosome 1 and 2 revealed by a voxelwise analysis of neuromelanin-sensitive MRI. *Hum. Brain Mapp.* **42**, 2823–2832 (2021).
26. Ohtsuka, C. et al. Changes in substantia nigra and locus coeruleus in patients with early-stage Parkinson's disease using neuromelanin-sensitive MR imaging. *Neurosci. Lett.* **541**, 93–98 (2013).
27. Schwarz, S. T. et al. The 'Swallow Tail' appearance of the healthy nigrosome—a new accurate test of Parkinson's disease: a case-control and retrospective cross-sectional MRI study at 3 T. *PLoS ONE* **9**, e93814 (2014).

28. Kim, J. M. et al. Loss of substantia nigra hyperintensity on 7 Tesla MRI of Parkinson's disease, multiple system atrophy, and progressive supranuclear palsy. *Parkinsonism Relat. Disord.* **26**, 47–54 (2016).

29. Blazejewska, A. I. et al. Visualization of nigrosome 1 and its loss in PD. *Neurology* **81**, 534–540 (2013).

30. Cosottini, M. et al. MR imaging of the substantia nigra at 7 T enables diagnosis of Parkinson disease. *Radiology* **271**, 831–838 (2014).

31. Guan, X. et al. Regionally progressive accumulation of iron in Parkinson's disease as measured by quantitative susceptibility mapping. *NMR Biomed.* **30**, https://doi.org/10.1002/nbm.3489 (2017).

32. Chen, Q. et al. Iron deposition in Parkinson's disease by quantitative susceptibility mapping. *BMC Neurosci.* **20**, 23 (2019).

33. Pyatigorskaya, N. et al. Comparative study of MRI biomarkers in the substantia nigra to discriminate idiopathic Parkinson disease. *Am. J. Neuroradiol.* **39**, 1460–1467 (2018).

34. Mazzucchi, S. et al. Quantitative susceptibility mapping in atypical Parkinsonisms. *NeuroImage Clin.* **24**, 101999 (2019).

35. Poston, K. L. et al. Substantia nigra volume dissociates bradykinesia and rigidity from tremor in Parkinson's disease: a 7 tesla imaging study. *J. Parkinsons Dis.* **10**, 591–604 (2020).

36. Schwarz, S. T. et al. T1-weighted MRI shows stage-dependent substantia nigra signal loss in Parkinson's disease. *Mov. Disord.* **26**, 1633–1638 (2011).

37. Schwarz, S. T., Xing, Y., Tomar, P., Bajaj, N. & Auer, D. P. In vivo assessment of brainstem depigmentation in Parkinson disease: potential as a severity marker for multicenter studies. *Radiology* **283**, 789–798 (2017).

38. Du, G. et al. Distinct progression pattern of susceptibility MRI in the substantia nigra of Parkinson's patients. *Mov. Disord.* **33**, 1423–1431 (2018).

39. Du, G. et al. Quantitative susceptibility mapping of the midbrain in Parkinson's disease. *Mov. Disord.* **31**, 317–324 (2016).

40. He, N. et al. Region-specific disturbed iron distribution in early idiopathic Parkinson's disease measured by quantitative susceptibility mapping. *Hum. Brain Mapp.* **36**, 4407–4420 (2015).

41. Bergsland, N. et al. Ventral posterior substantia nigra iron increases over 3 years in Parkinson's disease. *Mov. Disord.* **34**, 1006–1013 (2019).

42. Winkler, A. M., Ridgway, G. R., Webster, M. A., Smith, S. M. & Nichols, T. E. Permutation inference for the general linear model. *NeuroImage* **92**, 381–397 (2014).

43. Smith, S. M. & Nichols, T. E. Threshold-free cluster enhancement: addressing problems of smoothing, threshold dependence and localisation in cluster inference. *NeuroImage* **44**, 83–98 (2009).

44. Kim, E. Y., Sung, Y. H. & Lee, J. Nigrosome 1 imaging: technical considerations and clinical applications. *BJR* **8**, 20180842 (2019).

45. Massey, L. et al. 9.4 T MR microscopy of the substantia nigra with pathological validation in controls and disease. *Neuroimage Clin.* **13**, 154–163 (2016).

46. Friedrich, I. et al. Cell specific quantitative iron mapping on brain slices by immuno-μPIXE in healthy elderly and Parkinson's disease. *Acta Neuropathol. Commun.* **9**, 47 (2021).

47. Reimão, S. et al. Magnetic resonance correlation of iron content with neuromelanin in the substantia nigra of early-stage Parkinson's disease. *Eur. J. Neurol.* **23**, 368–374 (2016).

48. He, N. et al. Imaging iron and neuromelanin simultaneously using a single 3D gradient echo magnetization transfer sequence: combining neuromelanin, iron and the nigrosome-1 sign as complementary imaging biomarkers in early stage Parkinson's disease. *NeuroImage* **230**, 117810 (2021).

49. Greffard, S. et al. Motor score of the unified Parkinson disease rating scale as a good predictor of Lewy body–associated neuronal loss in the substantia nigra. *Arch. Neurol.* **63**, 584 (2006).

50. Wang, J. et al. Neuromelanin-sensitive magnetic resonance imaging features of the substantia nigra and locus coeruleus in de novo Parkinson's disease and its phenotypes. *Eur. J. Neurol.* **25**, 949–e73 (2018).

51. Matsuura, K. et al. A longitudinal study of neuromelanin-sensitive magnetic resonance imaging in Parkinson's disease. *Neurosci. Lett.* **633**, 112–117 (2016).

52. Castellanos, G. et al. Automated neuromelanin imaging as a diagnostic biomarker for Parkinson's disease. *Mov. Disord.* **30**, 945–952 (2015).

53. Matsuura, K. et al. Neuromelanin magnetic resonance imaging in Parkinson's disease and multiple system atrophy. *Eur. Neurol.* **70**, 70–77 (2013).

54. Ariz, M. et al. Dynamic atlas-based segmentation and quantification of neuromelanin-rich brainstem structures in Parkinson disease. *IEEE Trans. Med. Imaging* **38**, 813–823 (2019).

55. Wengler, K., He, X., Abi-Dargham, A. & Horga, G. Reproducibility assessment of neuromelanin-sensitive magnetic resonance imaging protocols for region-of-interest and voxelwise analyses. *NeuroImage* **208**, 116457 (2020).

56. Liu, K. Y. et al. In vivo visualization of age-related differences in the locus coeruleus. *Neurobiol. Aging* **74**, 101–111 (2019).

57. Betts, M. J., Cardenas-Blanco, A., Kanowski, M., Jessen, F. & Düzel, E. In vivo MRI assessment of the human locus coeruleus along its rostrocaudal extent in young and older adults. *NeuroImage* **163**, 150–159 (2017).

58. Lee, J. Y. et al. Multimodal brain and retinal imaging of dopaminergic degeneration in Parkinson disease. *Nat. Rev. Neurol.* **18**, 203–220 (2022).

59. Mitchell, T. et al. Emerging neuroimaging biomarkers across disease stage in Parkinson disease: a review. *JAMA Neurol.* **78**, 1262–1272 (2021).

60. Zhou, G. et al. Monitoring substantia nigra degeneration using free water imaging across prodromal and clinical Parkinson's disease. *Mov. Disord.* **38**, 774–782 (2023).

61. Maier-Hein, K. H. et al. Widespread white matter degeneration preceding the onset of dementia. *Alzheimers Dement.* **11**, 485–493.e2 (2015).

62. Ofori, E. et al. Increased free water in the substantia nigra of Parkinson's disease: a single-site and multi-site study. *Neurobiol. Aging* **36**, 1097–1104 (2015).

63. Pasternak, O. et al. Excessive extracellular volume reveals a neurodegenerative pattern in Schizophrenia onset. *J. Neurosci.* **32**, 17365–17372 (2012).

64. Schmidt, M. A. et al. Ultra high-field SWI of the substantia nigra at 7?T: reliability and consistency of the swallow-tail sign. *BMC Neurol.* **17**, 194 (2017).

65. Lehéricy, S., Bardinet, E., Poupon, C., Vidailhet, M. & François, C. 7 tesla magnetic resonance imaging: a closer look at substantia nigra anatomy in Parkinson's disease. *Mov. Disord.* **29**, 1574–1581 (2014).

66. Brammerloh, M. et al. Measuring the iron content of dopaminergic neurons in substantia nigra with MRI relaxometry. *Neuroimage* **239**, 118255 (2021).

67. Jin, L. et al. Combined visualization of nigrosome-1 and neuromelanin in the substantia nigra Using 3?T MRI for the differential diagnosis of essential tremor and de novo Parkinsonas disease. *Front. Neurol* **10**, 100 (2019).

68. Gramsch, C. et al. Nigrosome 1 visibility at susceptibility weighted 7 T MRI—a dependable diagnostic marker for Parkinson's disease or merely an inconsistent, age-dependent imaging finding? *PLoS ONE* **12**, https://doi.org/10.1371/journal.pone.0185489 (2017).

69. Fu, K. A., Nathan, R., Dinov, I. D., Li, J. & Toga, A. W. T2-imaging changes in the nigrosome-1 relate to clinical measures of Parkinson's disease. *Front. Neurol.* **7** (2016).

70. Sung, Y. H. et al. Differential involvement of nigral subregions in idiopathic parkinson's disease. *Hum. Brain Mapp.* **39**, 542–553 (2018).

71. Mahlknecht, P., Krismer, F., Poewe, W. & Seppi, K. Meta-analysis of dorsolateral nigral hyperintensity on magnetic resonance imaging as a marker for Parkinson's disease. *Mov. Disord.* **32**, 619–623 (2017).

72. Pavese, N. & Tai, Y. F. Nigrosome imaging and neuromelanin sensitive MRI in diagnostic evaluation of Parkinsonism. *Mov. Disord. Clin. Pract.* **5**, 131–140 (2018).

73. Ohtsuka, C. et al. Differentiation of early-stage parkinsonisms using neuromelanin-sensitive magnetic resonance imaging. *Parkinsonism Relat. Disord.* **20**, 755–760 (2014).

74. Oh, S. W. et al. Correlation of 3D FLAIR and dopamine transporter imaging in patients with Parkinsonism. *Am. J. Roentgenol.* **207**, 1089–1094 (2016).

75. Postuma, R. B. et al. MDS clinical diagnostic criteria for Parkinson's disease. *Mov. Disord.* **30**, 1591–1601 (2015).

76. Fahn, S., Elton, R. & UPDRS Development Committee. The Unified Parkinson's Disease Rating Scale. in *Recent Developments In Parkinson's Disease* (eds Fahn S, Marsden CD, Calne DB, Goldstein M) 15 3-163, 293-304. (Macmillan Health Care Information 1987).

77. Tomlinson, C. L. et al. Systematic review of levodopa dose equivalency reporting in Parkinson's disease. *Mov. Disord.* **25**, 2649–2653 (2010).

78. Priovoulos, N. et al. High-resolution in vivo imaging of human locus coeruleus by magnetization transfer MRI at 3 T and 7 T. *NeuroImage* **168**, 427–436 (2018).

79. Trujillo, P. et al. Contrast mechanisms associated with neuromelanin-MRI. *Magn. Reson. Med.* **78**, 1790–1800 (2017).

80. Acosta-Cabronero, J. et al. A robust multi-scale approach to quantitative susceptibility mapping. *NeuroImage* **183**, 7–24 (2018).

81. Jenkinson, M., Pechaud, M. & Smith, S. BET2: MR-based estimation of brain, skull and scalp surfaces. *Human Brain. Mapping.* **17**, 167 (2005).

82. Schofield, M. A. & Zhu, Y. Fast phase unwrapping algorithm for interferometric applications. *Opt. Lett.* **28**, 1194–1196 (2003).

83. Bilgic, B. et al. Fast quantitative susceptibility mapping with L1-regularization and automatic parameter selection. *Magn. Reson. Med.* **72**, 1444–1459 (2014).

84. Pei, M. et al. Algorithm for fast monoexponential fitting based on Auto-Regression on Linear Operations (ARLO) of data. *Magn. Reson. Med.* **73**, 843–850 (2015).

85. Tustison, N. J. et al. The ANTsX ecosystem for quantitative biological and medical imaging. *Sci. Rep* **11**, 9068 (2021).

86. Madelung, C. F. et al. Locus coeruleus shows a spatial pattern of structural disintegration in Parkinson's disease. *Mov. Disord.* **37**, 479–489 (2022).

87. Tustison, N. J. et al. N4ITK: improved N3 bias correction. *IEEE Trans. Med. Imaging* **29**, 1310–1320 (2010).

88. Fonov, V. et al. Unbiased average age-appropriate atlases for pediatric studies. *Neuroimage* **54**, 313–327 (2011).

89. Iglesias, J. E. et al. Bayesian segmentation of brainstem structures in MRI. *NeuroImage* **113**, 184–195 (2015).

90. Rua, C. et al. Substantia nigra ferric overload and neuromelanin loss in Parkinson's disease measured with 7 T MRI. *medRxiv* https://doi.org/10.1101/2021.04.13.21255416 (2021).

91. Prange, S. et al. Age and time course of long-term motor and nonmotor complications in Parkinson disease. *Neurology* **92**, e148–e160 (2019).

92. Zecca, L. et al. The role of iron and copper molecules in the neuronal vulnerability of locus coeruleus and substantia nigra during aging. *Proc. Natl Acad. Sci. USA* **101**, 9843–9848 (2004).

93. Keuken, M. C. et al. Effects of aging on T1, T2*, and QSM MRI values in the subcortex. *Brain Struct. Funct.* **222**, 2487–2505 (2017).

94. Bates, D. et al. lme4: linear mixed-effects models using "Eigen" and S4. https://cran.r-project.org/web/packages/lme4/index.html (2024).

Author contributions
Research project: A. Conception, B. Organization, C. Execution; Statistical Analysis: A. Design, B. Execution, C. Review and Critique; Manuscript: A. Writing of the first draft, B. Review and Critique. C.M: 1A, 1B, 1C, 2A, 2B, 3A S.F: 2A, 2B, 2C, 3B M.M: 2B, 3B VB: 1A, 1B, 3B K.M: 2A, 2B, 2C, 3B AH: 2C, 3B AL: 1A, 2C, 3D D.M: 1A, 1B, 1C, 2A, 2C, 3B HS: 1A, 1B, 2C, 3B.

Competing interests
The authors declare no competing interests.

Additional information
Supplementary information The online version contains supplementary material available at https://doi.org/10.1038/s41531-025-00972-7.

Correspondence and requests for materials should be addressed to David Meder or Hartwig R. Siebner.

Reprints and permissions information is available at http://www.nature.com/reprints

Publisher's note Springer Nature remains neutral with regard to jurisdictional claims in published maps and institutional affiliations.